

Research paper

Pressure core analysis of geomechanical and fluid flow properties of seals associated with gas hydrate-bearing reservoirs in the Krishna-Godavari Basin, offshore India



Junbong Jang^{a,*}, Sheng Dai^b, Jun Yoneda^c, William F. Waite^d, Laura A. Stern^e, Lee-Gray Boze^d, Timothy S. Collett^f, Pushendra Kumar^g

^a Integrated Statistics Inc., contracted to U. S. Geological Survey, Woods Hole, MA, United States

^b Georgia Institute of Technology, Atlanta, GA, United States

^c National Institute of Advanced Industrial Science and Technology, Sapporo, Japan

^d U. S. Geological Survey, Woods Hole, MA, United States

^e U. S. Geological Survey, Menlo Park, CA, United States

^f U. S. Geological Survey, Denver, CO, United States

^g Oil and Natural Gas Corporation, Panvel, Navi, Mumbai, India

ARTICLE INFO

Keywords:

National gas hydrate program expedition 02
Pressure core characterization tools
Gas hydrate-bearing sediments
Geotechnical properties
Seal layers

ABSTRACT

Physical properties of the sediment directly overlying a gas hydrate reservoir provide important controls on the effectiveness of depressurizing that reservoir to extract methane from gas hydrate as an energy resource. The permeability of overlying sediment determines if a gas hydrate reservoir's upper contact will provide an effective seal that enables efficient reservoir depressurization. Compressibility, stiffness and strength indicate how overlying sediment will deform as the in situ stress changes during production, providing engineering data for well designs. Assessing these properties requires minimally-disturbed sediment. India's National Gas Hydrates Program Expedition 2 (NGHP-02) provided an opportunity to study these seal sediment properties, reducing disturbance from gas exsolution and bubble growth by collecting a pressure core from the seal sediment just above the primary gas hydrate reservoir at Site NGHP-02-08 in Area C of the Krishna-Godavari Basin. The effective stress chamber (ESC) and the direct shear chamber (DSC) devices in the suite of Pressure Core Characterization Tools (PCCTs) were used to measure permeability, compressibility, stiffness and shear strength at the in situ vertical stress. Geotechnical properties of the predominantly fine-grained seal layer at in situ vertical stress are in typical clay sediment ranges, with low measured permeability (0.02 mD), high compressibility ($C_c = 0.26\text{--}0.33$) and low shear strength (404 kPa). Though pressure and temperature were maintained throughout the collection and measurement process to stabilize gas hydrate, the lack of effective stress in the pressure core storage chamber and the chamber pressurization with methane-free water caused core expansion and gas hydrate in a thin coarser-grained layer to dissolve. The PCCTs can reapply in situ stress with incremental loading steps during a consolidation test to account for sediment compaction. Gas hydrate dissolution can be limited by storing cores just above freezing temperatures, and by using solid spacers to reduce the storage chamber's free volume.

1. Introduction

Gas hydrate, which is most commonly found in nature as methane gas hydrate, is a crystalline solid composed of guest molecules (such as methane) in individual cages of water molecules (Sloan and Koh, 2007). In the marine environment, methane hydrate is stable at the low temperatures and high pressures found in continental slope and basin sediments. For the methane in gas hydrate to be economically viable as an

energy resource, however, gas hydrate must occur within a geologic reservoir structure capable of collecting, concentrating and retaining a significant volume of methane (Kvenvolden, 1993; Collett et al., 2009).

India's National Gas Hydrate Program Expedition 02 (NGHP-02) brought together seismic profiling, logging while drilling (LWD), in-situ testing and conventional/pressure core analyses to locate and study a variety of potential geologic reservoir structures, targeting gas-hydrate-bearing coarse-grained sediments offshore eastern India (See details in

* Corresponding author. U. S. Geological Survey, 384 Woods Hole Road, Woods Hole, MA, 02543, United States.

E-mail address: jjang@usgs.gov (J. Jang).

<https://doi.org/10.1016/j.marpetgeo.2018.08.015>

Received 17 April 2018; Received in revised form 10 August 2018; Accepted 14 August 2018

Available online 18 August 2018

0264-8172/ © 2018 Elsevier Ltd. All rights reserved.

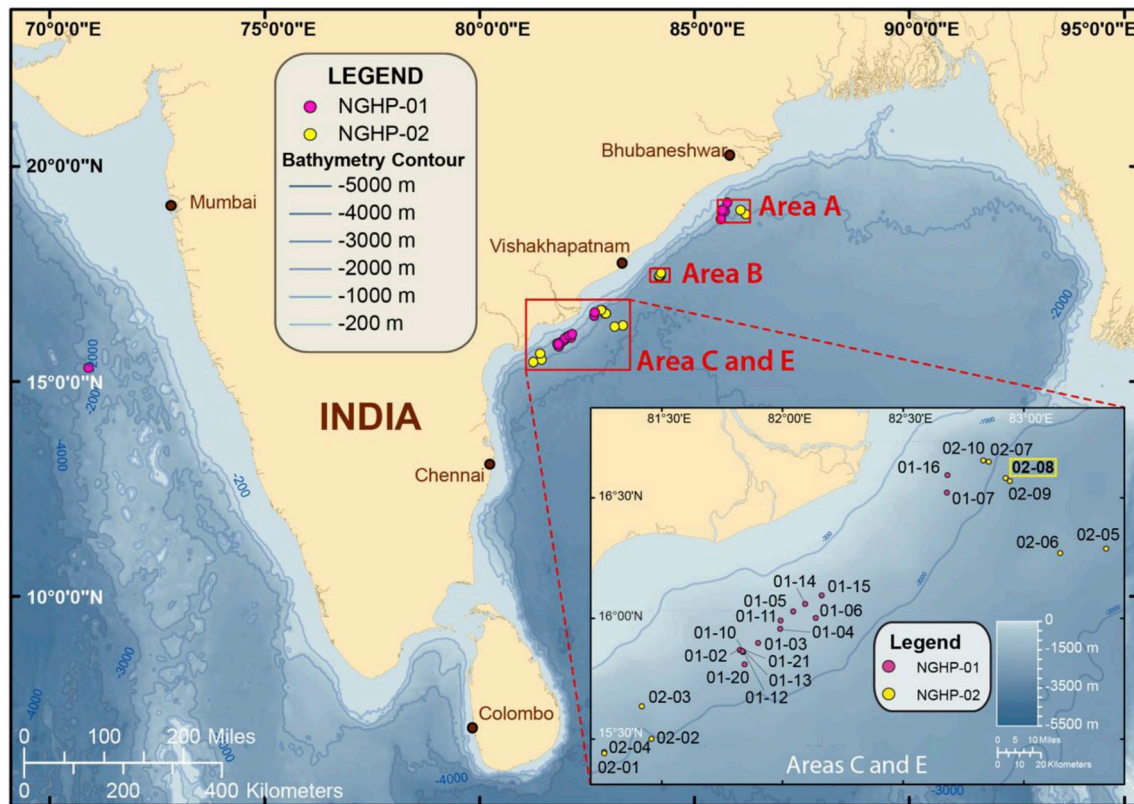


Fig. 1. India National Gas Hydrate Program (NGHP) site map, including drill site locations from the 2006 NGHP-01 and 2015 NGHP-02 expeditions (Collett et al., 2019; Kumar et al., 2019). Inset: Area C (upper right cluster of NGHP-02 sites) included coring through coarse-grained, gas hydrate-bearing sediment in a channel deposit (NGHP-02-07), levee deposits (Sites NGHP-02-08 and –09), and fan deposits (Site NGHP-02-05). This work analyses pressure-core sediment from the fine-grained seal above the coarse-grained levee deposits at Site NGHP-02-08 (inset site highlighted in yellow). (For interpretation of the references to colour in this figure legend, the reader is referred to the Web version of this article.)

Collett et al., 2019; Kumar et al., 2019; Shukla et al., 2019b). In Area C (Fig. 1), NGHP-02 identified gas hydrate reservoirs in a series of linked channel, levee and fan deposits along the mid-to-lower continental slope and floor of the Krishna Godavari Basin (Collett et al., 2019; Kumar et al., 2019; Shukla et al., 2019a). Of the four Area C sites that were pressure-cored, NGHP-02-08 and –09, characterized by levee deposits on either side of a buried channel, contained high gas hydrate saturations (Collett et al., 2019; Nanda et al., 2019; Waite et al., 2019). In particular, NGHP-02-09 was found to have coarse-grained hydrate-bearing sediments and also coarse-grained water-bearing sediments with an overall thickness of several tens of meters. This reservoir was modeled to assess its potential as an energy resource (Boswell et al., 2019a; Moridis et al., 2019).

Successfully extracting methane from a gas hydrate-bearing reservoir hinges in part on the properties of the overlying seal layer, and specifically, properties that evolve during production from the lower reservoir interval. In this study, the seal sediment's main geotechnical properties are measured: vertical permeability, compressibility, and shear strength. Vertical permeability is a critical parameter because low permeability seal sediment overlying a reservoir allows the reservoir to be more effectively depressurized to release methane (Ajayi et al., 2018). More generally, an effective overlying seal limits adverse effects on marine environments due to gas leakage through the seafloor (Dickens, 2001; Bohannon, 2008; Ruppel and Kessler, 2017).

Quantifying the seal's compressibility and strength are also important for engineering the production well to accommodate how sediment shifts with respect to the well casing during production. Though production is likely to be accomplished via a pore-pressure decrease that would favor increased effective stress and a resulting sediment compression, the response of the seal sediment to local changes in the

stress field is not necessarily always compressive (e.g. Lin et al., 2019). To accommodate the various possibilities for the stress-field evolution, compressibility tests run here also include the sediment response to a reduction in the effective stress and a reapplication of the effective stress.

Measuring these reservoir properties over the evolving stress conditions during production requires direct manipulation of minimally-disturbed sediment. Given the potential significance of the levee deposit gas hydrate reservoirs tested at NGHP-02-08 and –09, a pressure core was collected from the fine-grained, overlying sediment in contact with the coarse-grained reservoir at NGHP-02-08. Sites NGHP-02-08 and –09 have also been characterized based on seismic reflection data, LWD data, and shipboard and post-cruise sediment analyses, which provide geological and lithological information about the gas hydrate reservoir as well as the overburden and underlying sediments (Collett et al., 2019; Waite et al., 2019).

Although sediment disturbance still occurs during the pressure core collection (Dai and Santamarina, 2014), the capacity for pressure cores to preserve sediment at nearly in situ pore pressures allows gas hydrate-bearing sediment to be recovered intact. Even for sediments lacking gas hydrate, pressure coring ensures sediment is recovered without disrupting the fabric via gas exsolution and bubble expansion (Johns et al., 1982; Schultheiss et al., 2006). Due to technological advances made in pressure coring systems based on experiences from past drilling programs, pressure core analysis tools are now being more routinely deployed in conjunction with gas hydrate expeditions in the U. S. (Yun et al., 2006), India (Yun et al., 2010), Korea (Yun et al., 2011) and Japan (Priest et al., 2015; Santamarina et al., 2015; Yoneda et al., 2015, 2017; 2018 a; b; c). Post-recovery analytical capabilities for pressure cores have improved and expanded to enable reliable and systematic

measurement of physical, biological and geomechanical properties (reviewed by Boswell et al., 2019b; Dai et al., 2017).

This study utilizes the Effective Stress Chamber (ESC) and Direct Shear Chamber (DSC), which are part of the Pressure Core Characterization Tools (PCCTs) developed at the Georgia Institute of Technology (GaTech) and are now operated at the U. S. Geological Survey in Woods Hole. This work describes PCCT tests run on four subsections of the seal sediment pressure core from NGHP-02-08 at effective stresses ranging from in situ to ~10 MPa. After sediment was depressurized and the PCCT operations were concluded, three subsections from this pressure core were sent to GaTech for additional permeability, compressibility and stiffness testing at effective stresses up to ~25 MPa (Dai et al., 2019; Kim et al., 2019). Such high effective stresses are needed to simulate the projected reservoir depressurization requirements for extracting methane as an energy resource from these deepwater settings (Boswell et al., 2019a; Myshakin et al., 2019). Pressure core studies from coarse-grained NGHP-02 sediments carried out at the National Institute of Advanced Industrial Science and Technology (AIST) in Sapporo, Japan, are described by Yoneda et al. (2019a,b,c) and Oshima et al. (2019).

2. Pressure core NGHP-02-8B–30P: a seal layer from site NGHP-02-08 in area C

Seismic reflection data (Fig. 2) shows a buried channel-levee system in Area C, with Sites NGHP-02-08 and –09 penetrating levee deposits

on either side of the channel. At Site NGHP-02-08, the seismic images contain a strong peak amplitude reflection at ~2420 m below sea level (mbsl), or ~252 m below seafloor (mbsf). This reflector is inferred to be the target coarse-grained levee deposit (Collett et al., 2019; Shukla et al., 2019a,b). In the levee deposits, the major lithologic components are gravel, gravelly mud, and fine to coarse sand, intercalated with silty clay. Based on the LWD results from Hole NGHP-02-08A (Collett et al., 2019) the inference is made that, primarily between 246.8 and 272.0 mbsf, these coarse-grained sediments contain pore-filling gas hydrate that has formed interconnected networks within the existing pore space. The overlying fine-grained sediment hosts gas-hydrate-filled fractures in microfossil-rich clay sediments between 75 and 103 mbsf.

Pressure core NGHP-02-8B–30P was recovered from Hole NGHP-02-08B, located 15 m northwest of the LWD hole (Kumar et al., 2019). Had the core been collected from the LWD hole, the core recovery depth 246.7 to 247.8 mbsf (or 2414.2 to 2415.3 mbsl) would have bridged the seal/reservoir transition into highly gas hydrate-saturated reservoir sediment at ~247 mbsf. At Hole NGHP-02-08B, however, the top of the primary gas hydrate reservoir appears deeper, below the 248.1 mbsf depth at the base of core NGHP-02-8B–30P (Fig. 2). From shipboard visual core descriptions of adjacent sediment, this portion of the seal layer is lithologically characterized by gray to olive-black clayey silt with wavy or lenticular fine sand laminations. Quartz content is low, clay content is high, and pelagic microfossils are rare.

Pressure core scans of bulk density, compressional wave velocity (V_p) and X-ray images, Fig. 3, support the inference that pressure core

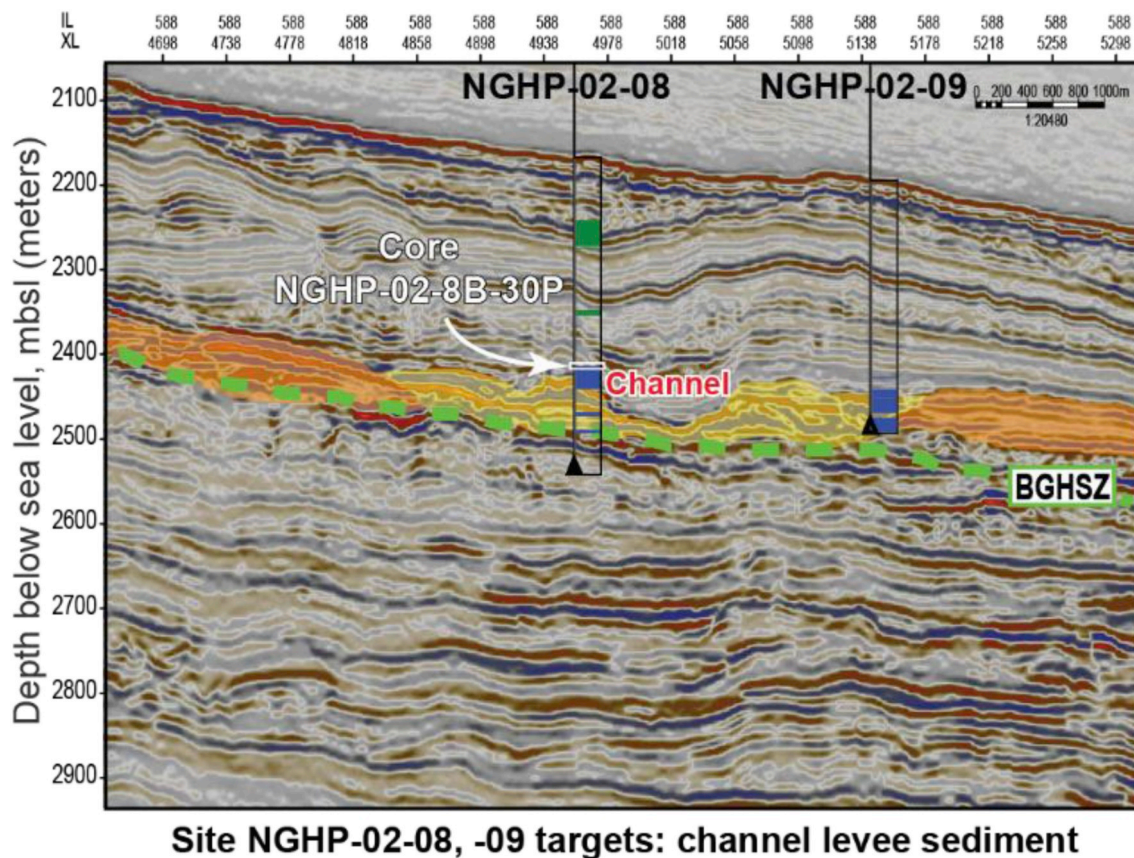


Fig. 2. Seismic reflection profile and geological structure for Sites NGHP-02-08 and –09 in Area C. Sites NGHP-02-08 and –09 penetrate the coarse-grained, sand-rich levee sediment (yellow) on either side of the buried channel. Further from the channel, the levees become coarse-grained, silt-rich sediment (orange). The total depths for boreholes at Sites NGHP-02-08 and –09 are 374 mbsf and 270 mbsf, respectively. Site NGHP-02-08 penetrates the base of the gas hydrate stability zone (BGHSZ, Collett et al., 2019), estimated to be at 323 mbsf (Collett et al., 2019; Waite et al., 2019). Two gas hydrate morphologies were observed at these sites: gas hydrate filled fractures in fine-grained sediment (green intervals to the right of the hole location) and pore-filling gas hydrate in the coarser-grained sediment (blue intervals) (Collett et al., 2019). The seal sediment tested in this work comes from pressure core NGHP-02-8B–30P, taken from just above the primary pore-filling gas hydrate interval. Site NGHP-02-08 water depth is 2167.5 m. (For interpretation of the references to colour in this figure legend, the reader is referred to the Web version of this article.)

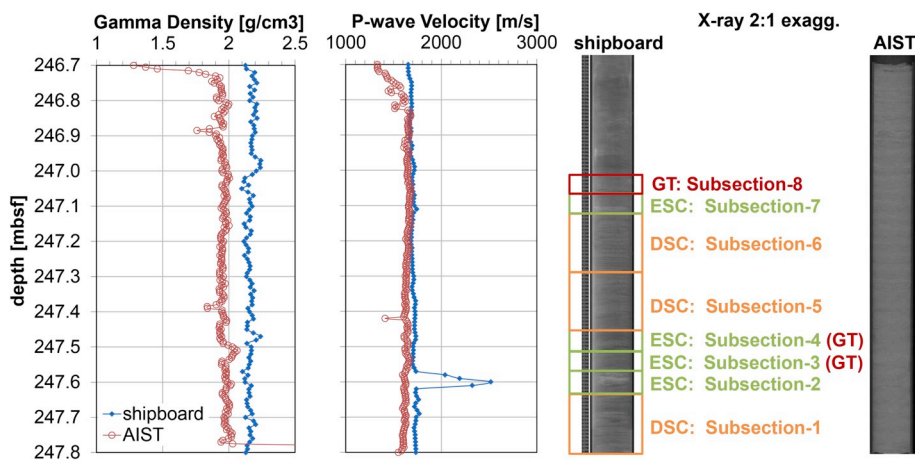


Fig. 3. Core logging information of pressure core NGHP-02-8B-30P from shipboard measurements using PCATS (Holland et al., 2019) and Pressure core Nondestructive Analysis Tools (PNATs) at AIST (Oshima et al., 2019). Gamma density profile indicates this seal-sediment core has a uniform lithology. At 247.6 mbsf, inferred fracture-filling gas hydrate in PCATS measurements is not apparent in PNATs measurements ~1 year later. Note that core images are presented here with the deeper portion at the bottom, but the cores are stored vertically in the opposite direction. Vertical storage allows gas hydrate-bearing fractures to close if gas hydrate dissolves. Pressure core nominal diameter is 50.8 mm (2 in.). The core is collected in a plastic liner (O.D. 59.6 mm and I.D. 53.6 mm), and the inside diameter of the storage chamber is 65 mm. Subsections were cut starting from the base of the core, and are listed numerically in the figure along with the testing device

that was utilized (DSC = Direct Shear Chamber, ESC = Effective Stress Chamber, GT = tested at Georgia Institute of Technology after depressurization).

NGHP-02-8B-30P is mostly uniform over its length, particularly over the tested subsections (defined in Fig. 3). Density results, though essentially uniform along the length of the tested portion of the core, are offset from each other. While a portion of this offset may be due to core expansion during storage, it is not known the extent to which the density difference are due to calibration differences between the two instruments.

Shipboard P-wave velocity measurements conducted through the core liner using the Pressure Core Analysis and Transfer System (PCATS, Holland et al., 2019) capture $V_p > 2000$ m/s at 247.6 mbsf, implying the presence of a thin gas hydrate occurrence. Even though the core was stored and transferred at low temperature ($\sim 5^\circ\text{C}$) and high pressure (~ 20 MPa), conditions well within the gas hydrate stability zone (~ 4.3 – 5 MPa at 5°C , depending on salinity as predicted by the CSMGem model (Ballard and Sloan, 2004), the V_p peak is absent in the scan performed a little over a year later. Correspondingly, gas hydrate is visible as a thin, horizontal white band on the shipboard PCATS X-ray image, but not on the AIST X-ray image. The pressure cores were stored using fresh, methane-free water as the pressure medium, so the loss of gas hydrate is likely due to gas hydrate dissolution in the water during long-term storage. Gas hydrate dissolution could be considered a new long-term sampling disturbance in which the gas hydrate content decreases during pressure core storage even when storage chamber parameters are well within the gas hydrate stability conditions.

3. Experimental methods: pressure core characterization tools, PCCTs

The PCCTs were designed to perform physical, geotechnical and biological experiments via direct manipulation of the pressure core sediment (Santamarina et al., 2012, 2015). For this study, we used the effective stress chamber (ESC) and the direct shear chamber (DSC) of the PCCTs to measure permeability, compressibility and shear strength, and to quantify how the fluid flow and deformation behavior of the seal sediment would evolve while methane was being extracted from the underlying reservoir. The ESC and DSC are shown schematically in Fig. 4. The core sub-section length for the DSC is ~ 16 cm and for the ESC, ~ 6 cm (Table 1). The nominal core diameter is 50.8 mm (2 in.).

Each test has two stages. During stage 1, PCCT experiments before depressurization, pore pressures are maintained at 10 MPa or above with syringe pumps (ISCO pumps 500D), and the chambers are operated in a refrigerated room ($\sim 4^\circ\text{C}$) to preserve the in situ phases, such as gas hydrate. These conditions are well within even the conservative gas hydrate stability field boundary of ~ 4.5 MPa predicted by CSMGem in the presence of seawater at that temperature. In stage 2, experiments after depressurization, the pore pressure is reduced to atmospheric to

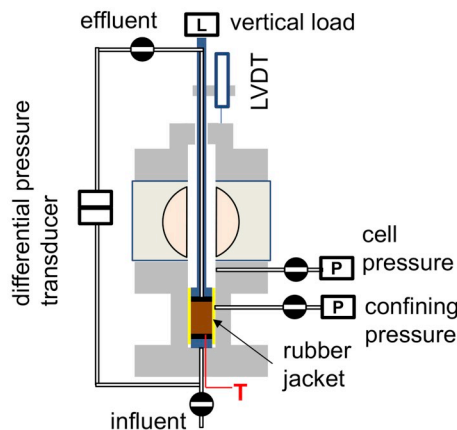
dissociate any gas hydrate present in the system. The stage 1 test sequences can then be repeated, but with atmospheric pore pressure. Because of the low pore-pressure, stage 2 testing can reach higher vertical effective stress (up to ~ 10 MPa) than can be obtained during stage 1.

3.1. Effective stress chamber, ESC: vertical permeability and compressibility

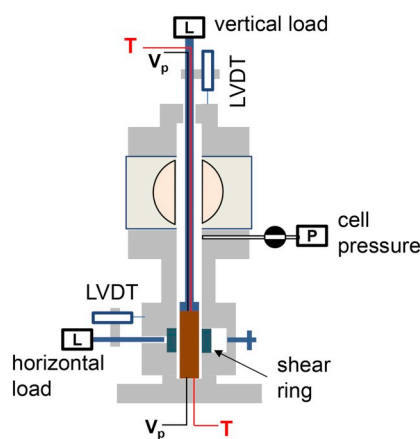
The ESC is equipped with a membrane frame to house a flexible rubber jacket that becomes the specimen's cylindrical boundary (Fig. 4a). With the top plunger contacting the specimen, the specimen is held top and bottom against porous stones, and a confining pressure can be applied to the outside of the membrane so the ESC can conduct a type of flexible wall permeability test (refer to ASTM D5084 (2010)). The ESC membrane cell has a gap of less than 1 mm between the rubber jacket and the surrounding steel wall. Though it is anticipated that vertical loading of the specimen causes the specimen to expand laterally and become confined as in a rigid-walled chamber, the flexible rubber jacket and modest confining pressure (maximum 50 kPa) ensure there is no preferential vertical flow along an open boundary on the specimen's cylindrical surface. Unless otherwise stated, "permeability" in this work is understood to mean "vertical permeability" with respect to the in situ geometry.

Using the ESC's vertical loading system, the in situ vertical stress is restored in several steps to prepare for the permeability and 1-D incremental loading consolidation tests (compressibility). The vertical stress (σ_v) applied to the specimen is $F/A-u_c$, where F is the vertical force, A is the specimen area, and u_c is the water pressure in the chamber (not the actual transient pore pressure). For the permeability test at an in situ vertical stress of 2 MPa, a constant differential pressure, Δp , is applied between the porous stones at the top and bottom of the specimen (Fig. 4). Differential pressures of 100, 200 and 300 kPa are used. The confining pressure on the rubber jacket is set to 50 kPa higher than the inlet pressure during the flow tests. Following the permeability test at the in situ stress state, the vertical stress can be increased in steps to perform a consolidation test along the specimen's virgin compression curve. Regardless of whether the gas hydrate is present in the subsection, each specimen undergoes depressurization, which is conducted while maintaining a constant 2 MPa vertical stress. Permeability and consolidation tests on depressurized specimens are repeated if necessary. With the pore pressure released, the specimen can be taken to higher effective stresses to extend the range of the compressibility test.

Of the four subsections that were cut from pressure core NGHP-02-8B-30P for the ESC, two subsections-2 and -4 (the locations are given in Fig. 3) are discussed here. Subsection-3 was shortened too much during the initial consolidation steps to conduct tests in the ESC, so this



(a) ESC



(b) DSC

Fig. 4. Experimental configurations of (a) the Effective Stress Chamber, ESC, used for compressibility and permeability measurements and (b) the Direct Shear Chamber, DSC, used for compressibility, shear strength and compressional wave velocity, V_p . Both tools operate within a load frame connected to a central plunger (blue vertical rod contacting the sample through an instruments cap) that passes through the tool's large ball valve to contact and apply vertical stress to the specimen (brown cylinder). Specimen dimensions are tracked with linear voltage displacement transducers, LVDT, and temperatures are tracked with thermocouples, T. (For interpretation of the references to colour in this figure legend, the reader is referred to the Web version of this article.)

material was packaged and sent to GaTech for additional study. Subsection-7 suffered a technical failure during the transfer into the ESC, and no data were recorded.

Subsection-2. Following a permeability test at 2 MPa vertical stress, 1-D incremental loading consolidation was conducted up to 6 MPa, then the sample was unloaded to 2 MPa for depressurization and dissociation. The consolidation time for each change in vertical load was allowed to run longer than 15 min, during which time elastic compression was completed, but the specimen was not fully consolidated (at least 40% consolidation was obtained, as determined from the coefficient of

consolidation described in Section 4.1). Permeability tests were conducted at 2 MPa and 6 MPa vertical stress before dissociation, and 2 MPa after dissociation, with no confining pressure due to the rubber jacket having been punctured. At 6 MPa vertical stress, the specimen had consolidated enough to reduce permeability to a level for which flow could only be obtained with $\Delta p = 300$ kPa, the maximum pressure difference allowed by the differential pressure gauge. The permeability measurement at 2 MPa after depressurization could not be completed because no flow could be detected even with $\Delta p = 300$ kPa. Following depressurization, a consolidation test was conducted from 2 MPa to

Table 1

Subsections of pressure core NGHP-02-8B–30P and experimental results from ESC and DSC (subsection numbers refer to Fig. 3).

Subsection No.		1	2	4	6
subsection length by depth [mbsf]		247.63–247.8	247.56–247.63	247.45–247.51	247.12–247.28
measurement chamber		DSC	ESC	ESC	DSC
consolidation indices	C_c	0.289	0.328 0.224 ^a	n/a	0.262
	C_s	0.023	0.062 0.028 ^a	n/a	0.003
	C_r	n/a	0.081 ^a	n/a	n/a
vertical permeability	at 2 MPa	n/a	$1.20 \times 10^{-17} \text{ m}^2$ (0.012 mD)	$1.22 \times 10^{-17} \text{ m}^2$ (0.012 mD)	n/a
	at 6 MPa		$4.64 \times 10^{-18} \text{ m}^2$ (0.005 mD)	n/a	

^a After depressurization.

9.2 MPa vertical effective stress, with several loading steps, then the vertical effective stress was returned to 2 MPa to compare the compressibility to that before depressurization.

Subsection-4. A slow set of consolidation steps was conducted up to the 2 MPa in situ vertical stress, where permeability tests were performed. Each loading step was maintained until displacement became a plateau, indicating consolidation completion. After the permeability test, the gas hydrate in the specimen was dissociated at the in situ effective stress to preserve the sediment fabric. The specimen was then packed for transfer to GaTech for horizontal and vertical permeability tests as well as additional consolidation tests at high vertical stress (see details in Dai et al., 2019; Kim et al., 2019).

3.2. Direct shear chamber, DSC: shear strength and compressibility

A DSC specimen is transferred into the DSC such that the specimen extends through a thick-walled shear ring (53.6 mm inner diameter; 53.59 mm height, 16.7 mm wall thickness), between the upper plunger and the bottom endcap (Fig. 4b). Similar to the ESC, the DSC vertical loading system applies vertical stress to the sample through the plunger for a consolidation test. The plunger and endcap are equipped with temperature sensors as well as compressional-wave transducers for measuring V_p . A direct shear test can be conducted by horizontally moving the shear ring in the middle of the specimen to generate a double-sided direct shear. For the shear test at 2 MPa in-situ vertical stress, the horizontal loading system controlled with an ISCO pump (500D) displaces the shear ring containing the middle section of the specimen by 10 mm (Fig. 4b) at a rate of 1.19 mm/min. At this rate, the test is considered an undrained shear test (Lambe, 1951). After resetting the shear ring, additional shear tests can be run at higher vertical stress after further consolidating the specimen. The additional consolidation moves the sheared interfaces down, allowing fresh sediment to be sheared in a subsequent test. If the additional consolidation does not reduce the specimen height, repeated shear tests will occur on the same shear planes, and results will reflect the sediment's residual shear strength. The specimen height is tracked by an LVDT (Fig. 4b), and a decrease in height will correspond to a decrease in void ratio (Fig. 5b). Void ratio (e) is the volume ratio of void (non-sediment) volume to solid volume in the soil, and porosity (n) is the volume ratio of void volume to total volume of the soil. The two parameters are related by $n = e / (1 + e)$. The P-wave measurements are reported for each consolidation step as well as before and after each shear test. As with the ESC, the specimen was dissociated via depressurization while holding vertical stress constant at 2 MPa.

We tested two subsections of pressure core NGHP-02-8B–30P in the DSC, subsection-1 and -6. Subsection 5 suffered a technical failure during the transition into the DSC and no data were recorded.

Subsection-1. This section is the deepest part of the pressure core (Fig. 3). A consolidation test was conducted while P-wave measurements were made at each loading step. During consolidation at the 2 MPa loading step, the specimen became too short to perform a shear test because the tip of the vertical loading plunger extended below the upper shear plane. The consolidation test was continued in steps to 6 MPa. After returning to 2 MPa vertical stress, the pore pressure was released for dissociation, and the experiment was terminated.

Subsection-6. A consolidation test was conducted up to 7 MPa vertical stress and unloaded to 2 MPa for dissociation. Each loading step was maintained until the displacement ceased changing, and shear tests were conducted at 2 MPa and 7 MPa during the loading and unloading steps. After the specimen was sheared at 2 MPa in-situ vertical stress, the shear ring and the sheared sediment segment in the specimen were returned to their original position. The additional loading steps increased vertical stress up to 7 MPa, and the second shear test was conducted. Due to sample shortening during the consolidation process, the designated shear planes at 7 MPa vertical stress were in different locations than the shear planes during the initial 2 MPa shear-strength

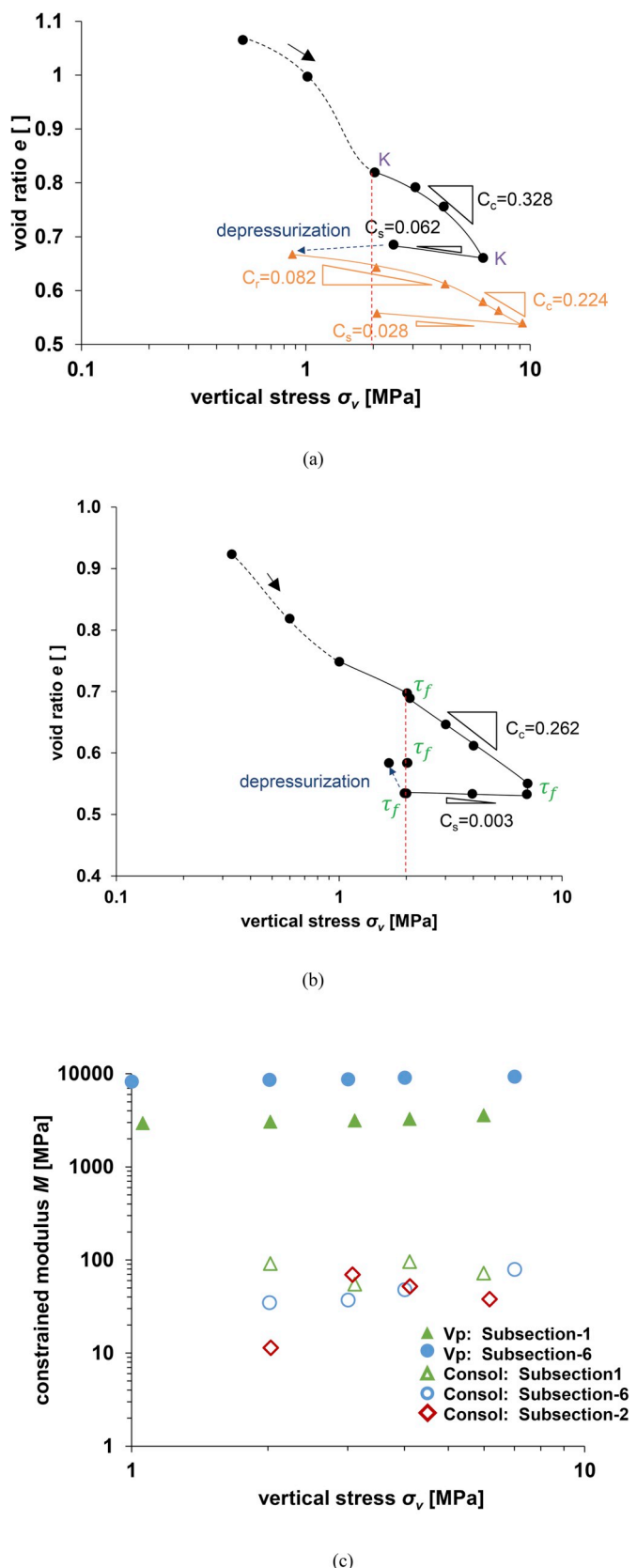


Fig. 5. Consolidation test results: (a) Subsection-2 (ESC), (b) Subsection-6 (DSC), (c) constrained modulus, M , determined for large strains with drained conditions by the coefficient of volumetric compressibility (M_{ss} , open symbols, Eq. (1)) and for small strains with undrained conditions by V_p measurements (M_{ss} , solid symbols, Eq. (2)). The data is available online (Jang et al., 2019).

test. The sheared segment was again returned to its original position after the 7 MPa shear, and the vertical stress was reduced to 2 MPa for dissociation. At 2 MPa, the specimen was sheared once before depressurization and twice after depressurization.

3.3. Fundamental physical properties and image analyses on dissociated specimens

Once a PCCT test is complete, the depressurized specimen is used to obtain a suite of index properties: grain density with a Quantachrome PentaPycnometer 5200e; specific surface by the wet method with methylene blue (Santamarina et al., 2002). Particle shape and mineralogy information are obtained via scanning electron microscopy (SEM) with energy dispersive spectroscopy (EDS) using a Tescan VEGA-3 variable-pressure SEM.

4. Results and analyses

Eight subsections were cut from pressure core NGHP-02-8B–30P (Fig. 3). Among them, the results from Subsections-1, -2, -4 and -6 are documented, here, with results and analyses on measured properties. Subsections marked as GT in Fig. 3 were transferred to Georgia Institute of Technology for further experiments of compressibility and permeability (Dai et al., 2019; Kim et al., 2019).

4.1. Geotechnical properties from PCCTs

4.1.1. Compressibility

Table 1 provides all the measured consolidation indices, and Fig. 5 plots the consolidation test results from the ESC Subsection-2 and DSC Subsection-6 tests. Significant void ratio changes in the early loading steps at vertical stresses less than 2 MPa indicate sediment disturbance occurring during long-term storage, transport and subsection cutting. In situ, these unconsolidated sediments are held together by the in situ effective stress, but it is only the hydrostatic stress (pore pressure) that is maintained in the pressure core collection and storage process. The lack of effective stress allows sediment to expand over time. This “stress relaxation” effect for NGHP-01 pressure cores is described by Dai and Santamarina (2014) and has been documented for pressure cores from Nankai Trough based on V_p results during pressure core loading tests by Santamarina et al. (2015). Sediment expansion can be exacerbated by swelling clays, which take up water at low confining stress. Also, in the absence of an abundant gas hydrate phase that provides cohesion (Yoneda et al., 2019b), observations through the clear-walled chambers at AIST show core subsection ends can slump as the subsection is cut. Taken together, these effects result in an initially loose sediment fabric, particularly at the subsection ends. The low-stress consolidation steps can reconsolidate the specimen, and the relatively large void-ratio decreases, associated with that initial consolidation to the in situ effective stress, can correspond to the extent of sediment disturbance. The V_p results from Santamarina et al. (2015) indicate the sediment expansion effects can be removed by consolidating the specimen back to its in situ effective stress.

The core site's geological history implies that there are no significant erosion and re-sedimentation as overconsolidation conditions in situ. The sediments represented in the core come from above the channel-levee system. They were deposited 2–3 million years ago, and have since endured natural seafloor fluctuations that would not have over consolidated the sediment and introduced an unloading process. Deep subsurface sediment tends to be normally consolidated (Chen and Mayne, 1994), and the Site NGHP-02-08 LWD-based porosity trend with depth is consistent with a normally consolidated deposit (Waite et al., 2019).

Given their 246 mbsf in situ subsurface depth, these subsections would require at least 2 MPa vertical stress to return to their in situ vertical effective stress and begin virgin compression. Thus, the virgin

compression index C_c is calculated using the consolidation data above 2 MPa vertical stress. Because the ESC consolidation test of Subsection-4 was conducted only up to 2 MPa, the compression index of Subsection-4 is not calculated. The rebound (or swelling) index C_s , and recompression index C_r , are calculated using the void ratio changes during unloading, C_{ss} , and reloading, C_r . Indices from consolidation tests are calculated from $-\Delta e/\Delta \log \sigma_v$, where e is the void ratio.

Subsection-6 test results yield $C_c = 0.262$ and $C_s = 0.003$ for complete consolidation at each loading step. Subsection-1 and -2 have consolidation indices higher than those of Subsection-6 (see the values of each section in Table 1 and Fig. 5a and b), and the higher indices can be associated with additional sediment disturbance processes experienced by Subsections 1 and 2.

One source of disturbance is related to the sediment mineralogy and exposure to fresh water. Based on the mineralogy from SEM-EDS results (Section 4.2) and from shipboard smear slide data in same lithologic unit, this core contains clay minerals (~50%) that can swell in response to fresh water and the lack of vertical effective stress (Bolt, 1956; Sridharan and Rao, 1973). Subsections -1 and -2 are close to the portion of the core where the compressional wave velocity scans indicate gas hydrate decomposed (Fig. 3). The loss of the gas hydrate layer freshens the surrounding water and leaves void space that increases the sediment compressibility. The situation is exacerbated in Subsection 1, because whereas Subsections 2-6 are confined top and bottom by sediment within the core, Subsection 1 is the bottom end of the core with its lower face exposed directly to the fresh pressurization water. Consequently, Subsection 1 has the entire core-storage period to expand out of the core liner. Moreover, during the test of Subsection-1, the bottom of Subsection-1 partially extruded from the DSC sample space, penetrating into the connected pressure and flow lines. This extrusion appears as a shortening of the specimen that is misinterpreted as a void ratio decrease.

These core expansion processes cause the sediment void ratio at the start of testing to be higher than that of the original fabric. The void ratio of Subsection-1 at 2 MPa ($e_{2MPa, loading} = 1.458$) is the highest, and the void ratio at 2 MPa for each subsequent subsection decreases as the subsection gets closer to Subsection-6. A high initial void ratio could result in the compression index being overestimated since the compression index scales with the initial void ratio (Burland, 1990; Sridharan and Nagaraj, 2000; Cerato and Lutenegeger, 2004; Tiwari and Ajmera, 2011).

The coefficient of volume compressibility, m_v , for Subsection-6 is calculated at each loading step via:

$$m_v = -\frac{\Delta e/\Delta \sigma}{1 + e_i} = \frac{1}{M_{ls}}, \quad (1)$$

where e_i is the void ratio at the beginning of the loading step. The constrained modulus M is the reciprocal of m_v , and is used here to capture the large-strain modulus, M_{ls} .

The constrained modulus can also be calculated from V_p measured during each loading step:

$$M_{ss} = \rho_b V_p^2, \quad (2)$$

where the ρ_b is the bulk density. Here, the constrained modulus M_{ss} captures the high-frequency, small-strain sediment response. The $M_{ss} = 8.6$ GPa (8600 MPa) calculated from the V_p measurement (Eq. (2)) is much higher than the 35 MPa M_{ls} value obtained by the consolidation test at 2 MPa in situ vertical stress for Subsection-6 (Eq. (1)). This discrepancy is because M_{ls} is obtained from large-strain, inelastic deformations that are slow enough for pore pressures to equilibrate. In contrast, M_{ss} pertains to small-strain, instantaneous (undrained) linear elastic deformations that do not induce any soil fabric change. Thus, if a reservoir simulation entails large deformations (strains of ~0.1–1%; Mitchell and Soga, 2005), M_{ls} from the consolidation test would be the proper input parameter for the simulation.

Using the square-root time method (Taylor, 1948), the coefficient of consolidation c_v for Subsection 6 at 2 MPa is $2.53 \times 10^{-7} \text{ m}^2/\text{s}$. This value falls within the expected range for undisturbed clay sediments (NAVFAC, 1986). Due to porosity reduction, c_v tends to decrease as the vertical stress increases. From Terzaghi's consolidation theory, the hydraulic conductivity k can be determined:

$$k = c_v m_v \gamma_w \tag{3}$$

where γ_w [kN/m^3] is the unit weight of water. For this subsection, application of (3) yields $k = 4.99 \times 10^{-10} \text{ m/s}$ (converted to $5.09 \times 10^{-17} \text{ m}^2$ or 0.052 mD).

4.1.2. Permeability

Subsections-2 and -4 were dedicated to permeability tests along the vertical direction through the sediment. Permeability K [m^2] is obtained from Darcy's law:

$$K = \frac{q}{\nabla p / \mu} \tag{4}$$

where the q [m/s] is fluid flux, ∇p [Pa/m] is the pressure gradient, and μ [$\text{Pa}\cdot\text{s}$] is the fluid viscosity (taken here to be $1.5 \times 10^{-6} \text{ kPa}\cdot\text{s}$ for pure water at 5°C (Young et al., 2007)). Permeability was measured at the estimated in situ vertical stress, 2 MPa ($e = 0.082$), as well as at 6 MPa ($e = 0.661$) for Subsection-2 (Table 1). As the pore sizes and void ratio decreased during consolidation, permeability decreased. At 6 MPa, the maximum 300 kPa differential pressure was required to provide measurable flow.

A slight permeability drop would have occurred due to the void ratio decrease during depressurization (Fig. 5a), but the formation of gas bubbles in the pore space as methane exsolved from the pore fluid during depressurization would more significantly decrease the specimen permeability for water. Subsection 2 generated 1100 cm^3 of gas at atmospheric pressure during depressurization, and was the only subsection to generate a measurable volume of gas. In the presence of even small gas concentrations (10–15%), the permeability for water can drop by a factor of two relative to the permeability in a gas-free system (Brooks and Corey, 1964; Kurihara et al., 2011; Reagan and Moridis, 2008; Santamarina et al., 2015). This gas-induced permeability decrease provides strong motivation for obtaining pressure cores, which retain the in situ phases and allow measurements such as permeability to be conducted while avoiding the specimen disturbance caused by gas coming out of solution during the depressurization experienced by conventional cores.

Permeability tests on Subsection-4 were conducted only at 2 MPa vertical stress (Fig. 6). The measured void ratio (0.9) of Subsection-4 at 2 MPa was larger than that (0.82) of Subsection-2, but the permeability of the two subsections was similar. After depressurization, this specimen was used to study permeability anisotropy (see details in Dai et al., 2019). The vertical permeability measured by Dai et al. (2019) at 2 MPa was $3.14 \times 10^{-17} \text{ m}^2$ (0.032 mD), at 0.87 void ratio, in agreement with both the Subsection-2 and -4 results (0.012 mD). Priest et al. (2019) ran a shipboard vertical permeability test through a pressure-maintained subsection of this pressure core at 247.92 mbsf, 12 cm deeper than the base of the pressure core section studied in this work. Their result was 0.0013 mD, measured at a comparable 1.96 MPa vertical stress. No void ratio is reported in their study, however from the original shipboard PCATS density scan, the entire core is expected to be quite uniform. These direct measurements of permeability are also comparable with the Subsection-6 estimate of 0.052 mD from Terzaghi's 1-D consolidation theory (Eq. (3)). Based on approximately the order-of-magnitude agreement between the direct measurements, which utilize independent tools and methodologies, a consensus permeability estimate of 0.02 mD is proposed for a 0.85 void ratio and at the in situ vertical stress of 2 MPa. This permeability is low enough to be considered as practically impermeable clay (Terzaghi et al., 1996).

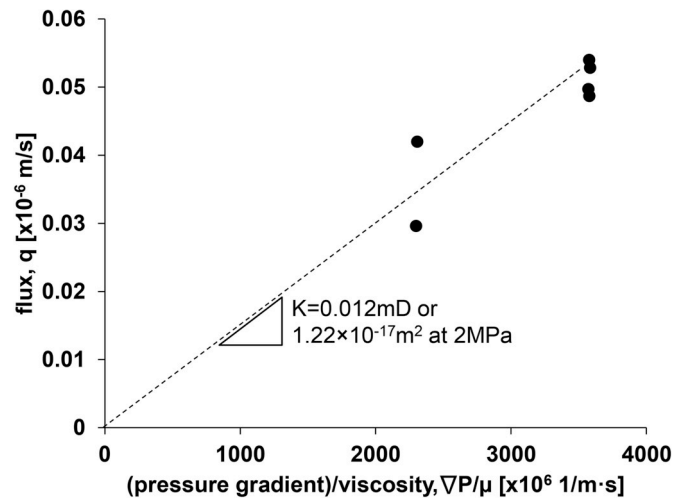


Fig. 6. Vertical permeability test results of Subsection-4 using the ESC. The data is available online (Jang et al., 2019).

4.1.3. Shear strength

Subsection-6 was subjected to undrained shear strength tests as a function of the vertical stress history, and Table 2 summarizes the measured shear strength (τ_f) and the friction angle values. Both parameters are dependent on the shear surface condition at a given overburden stress. Fig. 7a shows the normalized stress-strain curves.

For the virgin loading steps, a peak shear strength is observed during the direct shear tests at 2 MPa and 7 MPa vertical stress. The peak friction angle, ϕ_{peak} , is obtained at that peak shear strength. The peak shear strength increases with increasing vertical stress (Table 2). With increasing horizontal strain after the peak shear strength is reached, the shear stress decreases, flattening into the plateau (Fig. 7a). The ultimate friction angle, ϕ_u , is defined at 0.125 horizontal strain within that stress-strain curve plateau. The peak friction angle of 11° and ultimate friction angle of 8.5° are as low as those of montmorillonite (Mesri and Olson, 1970; Lupini et al., 1981; Mesri and Cepedadiaz, 1986).

In Fig. 7a, the normalized curves at 2 MPa and 7 MPa vertical stress are alike, but the vertical strain during the two direct shear tests shows different behaviors. The specimen at the in situ 2 MPa vertical stress does not become contractive until 0.007 horizontal strain, but at 7 MPa the specimen is contractive throughout the test. The change in the vertical strain behavior is associated with a fabric change in the shear band: the platy particle orientation on the shear plane tends to become

Table 2

Shear strength measurements: Subsection-6 (pressure core NGHP-02-08B–30P, 247.12–247.28 mbsf).

applied vertical stress, σ_v [MPa]	virgin loading		unloading		
	before depressurization		after depressurization		
	2.1	7.0	2.0	2.0	2.0
peak shear stress [kPa]	403	1292	n/a		
peak friction angle, ϕ_{peak} [°]	11.0	10.5			
yield shear stress [kPa]	n/a		627	n/a	218
friction angle at yield, ϕ_{yield} [°]			17.4	6.2	
shear stress at 0.125 of horizontal strain	287	1090	748	441	283
ultimate friction angle at 0.125 of horizontal strain, ϕ_u [°]	7.9	8.9	20.5	12.3	8.0

Remark: friction angle $\phi = \tan^{-1}(\tau/\sigma_v)$.

parallel to the shear plane during the shear test, allowing the vertical strain to be contractive (Skempton, 1964; Lupini et al., 1981). In the case of vertical strain at 7 MPa loading, high vertical stress can induce additional destructuring of the in situ fabric and additional volume contraction during the shear test.

After the Subsection-6 specimen is unloaded from 7 MPa to 2 MPa (Fig. 5b), the shear strength curve alter to work-hardening with contractive vertical strain, and no peak friction angle is observed in the shear test before depressurization (Fig. 7a). The stress-strain curve alteration may be because the shear planes are the same as the shear

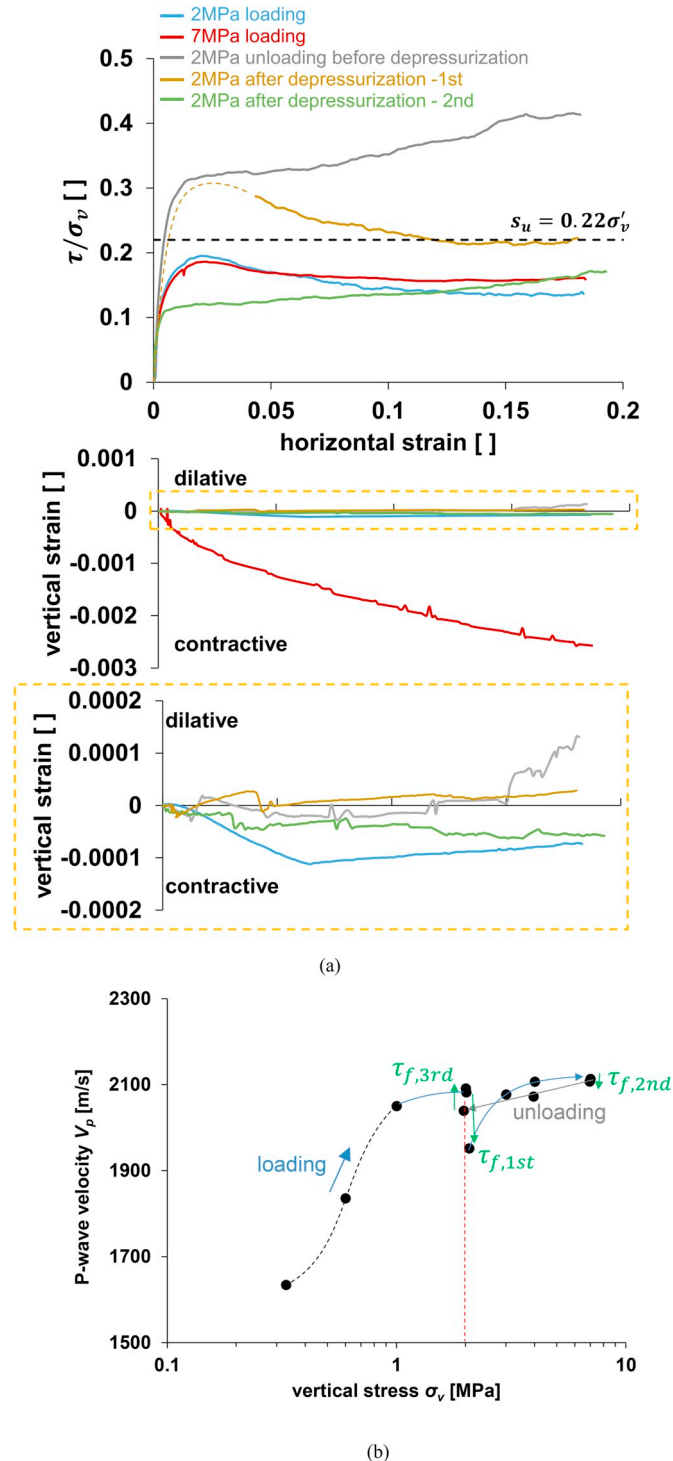


Fig. 7. Direct shear test results in DSC: (a, upper panel) normalized stress-strain curves, with the y-axis given as the ratio of shear stress τ to applied vertical stress σ_v . The empirical relationship between the undrained shear strength, s_u , and vertical effective stress, σ'_v , from Mesri (1989) is shown by the horizontal dashed line. (a, middle panel) vertical versus horizontal strain curves from Subsection-6, showing dominantly contractive behavior only for the 7 MPa virgin loading case. Lower panel zooms in on the gold-dashed region from the middle panel; (b) V_p as measured for each vertical loading step in the consolidation test and direct shear test (τ_f – shear test, numbered in the order in which they occurred). Blue curves indicate loading, gray indicates unloading, and the vertical dashed red line indicates the in situ vertical stress. Black dashed curve indicates the V_p increase as the applied vertical stress reconsolidates the specimen to its in situ stress ratio, which increased via to stress relaxation and sediment expansion due to the absence of any vertical effective stress in the storage chamber. The data is available online (Jang et al., 2019). (For interpretation of the references to colour in this figure legend, the reader is referred to the Web version of this article.)

planes of the 7 MPa shear test due to the minimal rebound of the specimen height during unloading in the consolidation test (Fig. 5b).

After depressurization, two shear tests were conducted with Subsection-6. The first test shows only the ultimate friction angle because the early part of the shear test was missed due to a technical failure. The strain curve shows dilatative vertical strain during the test. Based on the measured stress and strain data, the stress-strain curve would include a peak point and become a plateau at larger strain. In the second shear test after depressurization, the stress-strain curve is work-hardening with contractive vertical strain, and the shear strength at 0.125 horizontal strain is 65% of that of the first test because the shear planes in the second test are the same as the first test planes (Fig. 5b). The second test prompts additional fabric disturbance within the shear band beyond what occurred in the first test. Accordingly, the ultimate friction angle (8°) of the second test can be considered as a residual friction angle.

The variation of V_p with vertical stress (Fig. 7b) reflects the loading steps of the consolidation and the shear band generation during each shear test. V_p increases as the intergranular contacts stiffen due to increased vertical loading. However, each shear strength test generates two shear bands in the specimen, and shear bands can delay P-wave propagation by disrupting the sediment fabric and destroying stiff connections between sediment particles. V_p decreases 6.3% after the first shear test at 2 MPa vertical stress, for instance. The minimal reduction (0.3%) of V_p after the shear test at 7 MPa vertical stress (Fig. 7b) may be due to the comparatively large volume contraction creating additional stiff sediment-sediment contacts during the shear test that offset the effect of the shear bands on V_p . The shear test at 2 MPa after the unloading step but before depressurization, $\tau_{f,3rd}$, shows a 2.6% increase in V_p . This may be due to the late dilatative volume change which prompts the pore water pressure within the shear bands to decrease, locally increasing the effective stress and V_p (Todd and Simmons, 1972).

4.1.4. Gas hydrate occurrence and saturation

Each subsection was depressurized while maintaining 2 MPa vertical stress to dissociate any gas hydrate and to retain the sediment fabric for post PCCT sample characterization studies. From Fig. 3, no gas from gas hydrate should be expected except in or near Subsection-2, where the shipboard X-ray image indicates a thin, horizontal gas hydrate occurrence existed at the time of recovery. As noted above, the gas hydrate itself appears to have dissolved during storage prior to the AIST X-ray scan, but Subsection-2 produced 1100 cm³ of gas, and was the only subsection to produce a measurable quantity of gas. Assuming all gas collected had previously been held in gas hydrate, the total pore-space gas hydrate saturation for the 7 cm-long Subsection-2 would have been ~10%. Upon examining the subsection after extracting it from the ESC, a horizontal layer of coarser-grained sediment was observed

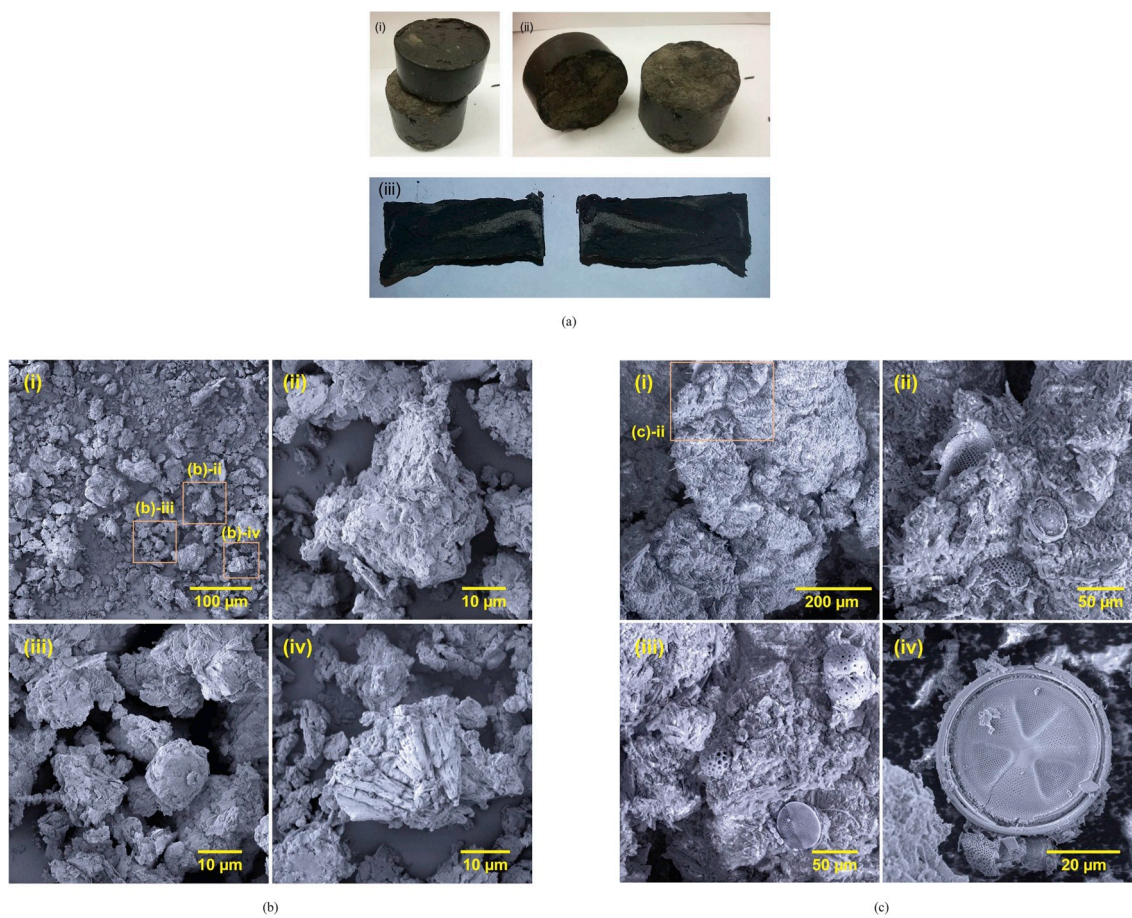


Fig. 8. Core and sediment grain imagery: (a) A part of Subsection-6 cleaved by hand: the horizontal split in (i) and (ii) shows evidence of a silty-fine-grained layer (light areas on the top of the lower section), (iii): both halves showing a second silty fine-grained layer in cross section (symmetric light streak within both halves of the dark, fine-grained specimen); (b) SEM-EDS images of fines from the seal layer core studied here, Core NGHP-02-08–30P, Area C – (i) sediment at low magnification, indicating locations of the other images in (b). (ii) “grain” that is really a cluster of fines, (iii) fine quartz particles coated by clay minerals, (iv) organic material with calcium carbonate; (c) for comparison, SEM-EDS images of fines in the seal layer above the primary gas hydrate reservoir in Area B, Core NGHP-02-23C–10P are shown here – (i) particles at low magnification showing the abundant diatoms and the location of image ii, (ii) and (iii) show examples of diatoms and microfossil shards, (iv) a diatom. The low microfossil content in the Area C, NGHP-02-08 seal sediment (b) relative to that in the Area B, NGHP-02-23 seal sediment (c) improves the effectiveness of the NGHP-02-08 seal, lowering both the porosity and permeability relative to that observed above the primary Area B gas hydrate reservoir (Jang et al., 2019).

(analogous to the layer from Subsection-6 (Section 4.2, Fig. 8a)). The collected gas is inferred to be biogenic methane based on its light isotopic ratio $\delta^{13}\text{C}-\text{CH}_4$ ($< 60\text{‰}$), which is in agreement with the shipboard downhole isotopic profile (Collett et al., 2019; Dixit et al., 2019).

4.2. Depressurized specimen

Fig. 8a shows Subsection-6 after depressurization in the DSC. Even though the specimen became stiff during consolidation and could hold its shape, it was plastic and cohesive like a clay sediment. The specimen could be split vertically and horizontally by hand, and the specimen split surface in the horizontal direction revealed the non-plastic, silty fine particle layer shown in Fig. 8a–i and –ii. When the specimen was split vertically, the split surface texture was rough, and the thin interbed could be observed on the cross-sectional face (Fig. 8a–iii).

SEM-EDS images in Fig. 8b provide details of the fine particle shapes, the variety of clustering behavior and the mineralogy observed in this core. Clay minerals and small fines can cluster as a lump (Fig. 8b–ii) since the fabric of fines can be dominated by electrical interparticle forces between fines (e.g. Jang et al., 2018). Quartz-type fines are observed to be coated with clay or mica particles (Fig. 8b–iii). Fig. 8b–iv shows a fragment of organic material or microfossil, with SEM-EDS confirmation of calcium carbonate in the fragment.

Fundamental physical properties are measured on depressurized specimens to characterize the sediments after they have been tested in the PCCT. For Core NGHP-02-08B–30P, the fine-grained lithology with thin layers of silty sediment was assumed to be consistent throughout the core. Although the AIST X-ray image in Fig. 3 does not show significant heterogeneity in the core, physical properties from depressurized sediment show the core does have localized heterogeneous as shown Fig. 8a. From the PCATS shipboard scan (Fig. 3), only the thin, coarser layer at 247.6 mbsf appeared to be gas hydrate-bearing, meaning not all of the coarser layers in the core have effective connections to a methane supply.

Fundamental properties measured for Subsection-5 are: specific surface, $167\text{ m}^2/\text{g}$; grain density, $2.66\text{ g}/\text{cm}^3$; median grain size d_{50} , $68.37\text{ }\mu\text{m}$; and in situ water content, 0.34. For comparison, the median grain size d_{50} is $7.9\text{ }\mu\text{m}$ and the liquid limit is 60.6 for the Subsections tested at GaTech (see details in Dai et al., 2019). From the shipboard data of the specimen adjacent to pressure core NGHP-02-8B–30P (less than 1 m above the top of the core), smear slide analysis suggests a mineralogy of low quartz content (10%) and high clay content ($> 50\%$) with low organic material content ($\sim 5\%$). The shipboard grain size measurement yields $d_{50} = 12.27\text{ }\mu\text{m}$.

The high specific surface is due to the small grain size and the observed platy clay or mica particles, which are observed to cluster as a

lump (Fig. 8b–ii) but can also coat quartz particles (Fig. 8b–iii). Organic materials or microfossils, though not abundant in this sediment, also contribute to the high specific surface with their internal void surfaces (Fig. 8b–iv). The microfossil content (~5%) in the seal layer at Site NGHP-02-08 is less than that (~20%) in the seal layer above Area B's primary gas hydrate reservoir (e.g. Site NGHP-02-23). As Fig. 8 b and c demonstrate, this difference is large enough to be easily observed in the SEM scans. No direct measurements of the seal sediment permeability is available above Area B's primary gas hydrate reservoir, but comparisons of microfossil content and porosity, both of which are lower in Area C Site's NGHP-02-08 and -09 than in Area B, suggest that the NGHP-02-08 and -09 seal sediment provides the more effective barrier to fluid migration at the upper boundary of the gas hydrate reservoir (Jang et al., 2019; Waite et al., 2019). Loss of methane through the upper seal via fluid migration may play a role in how a reservoir develops (Waite et al., 2019), but as shown by Ajayi et al. (2018), a more significant consequence from an energy resource perspective is that a low seal permeability is critical for establishing an effective depressurization of the gas hydrate reservoir itself to extract the methane.

5. Discussion and implications

5.1. Permeability

For Site NGHP-02-08, a consensus in situ vertical permeability estimate of 0.02 mD has been derived from consolidation tests and from direct measurement of flow through sediment from pressure core NGHP-02-08B–30P using the PCCT analysis described here, using direct flow testing in the shipboard PCATS Triaxial system (Priest et al., 2019), and using a separate double-ring permeameter (Dai et al., 2019) on sediment depressurized at the in situ effective stress in the PCCT to preserve the in situ fabric. These tests were all run at the in situ vertical effective stress, and the measurements by this study and by Priest et al. (2019) were made on pressure cores prior to depressurization. Because no gas hydrate was inferred to exist at the GaTech subsection depths (Fig. 3), the GaTech measurement was made in a water-saturated condition with no gas hydrate present. Together, these measurements provide a consensus estimate of the in situ vertical permeability just above the primary gas hydrate reservoir at NGHP-02-08.

It is instructive to compare the consensus estimate of the in situ vertical permeability derived from direct measurements to available indirect estimates of permeability. Here, the consensus permeability estimate is compared with estimates inferred from 1) index property analyses of recovered sediment, and 2) LWD Nuclear Magnetic Imaging (NMR) results.

If fine-grained sediment is recovered, an index property-based permeability estimate can be obtained by following the empirical approach of Carrier (2003) and Ren and Santamarina (2018). Permeability can be estimated from the specific surface (S_v) and void ratio, and for the 167 m²/g specific surface and ~0.85 void ratio measured here, the predicted permeability would be 0.0002–0.0004 mD. This is two orders of magnitude smaller than the experimental consensus value. One contribution to this discrepancy comes from how the approach of Ren and Santamarina (2018) emphasizes pore size as a fundamental control on permeability. If the in situ sediment fabric has larger pores than expected for the given void ratio and sediment specific surface due to clustered fines, for instance, the measured permeability can exceed that of empirical fits derived from natural and remolded samples.

This inferred relationship between sediment fabric and pore size highlights the importance of making permeability measurements on minimally-disturbed in situ sediment fabric. Regarding tests done on depressurized sediment after pressure core analyses, the need to maintain the sediment fabric suggests that, for best results, specimens should be dissociated or depressurized while maintaining the in situ effective stress to prevent disaggregation and disruption of the sediment fabric.

In contrast, the LWD NMR downhole permeability estimate, 0.3 mD, for the recovered depth of the core described here (Collett et al., 2019; Waite et al., 2019), is a little more than an order of magnitude larger than the direct measurement results. The Schlumberger Doll Research calculation of permeability from NMR data contains an empirical multiplicative prefactor to obtain the permeability, k_{SDR} . In NGHP-02, as in previous field studies, this empirical multiplicative factor was set to 4 mD/msec². This prefactor was used in the Nankai Trough gas hydrate study (Fujii et al., 2015), and is also commonly applied to non-gas hydrate studies of sandstone (Daigle and Dugan, 2011). As Daigle and Dugan (2009, 2011) show, this prefactor can be shown to be inversely dependent on the sediment specific surface. For fine grained, high specific surface sediments, the prefactor should be reduced by as much as two orders of magnitude (Daigle and Dugan, 2011), which directly reduces the permeability estimate by the same factor.

An additional issue for interpreting NMR permeabilities is that k_{SDR} is not a directional permeability measurement. The result depends on the inferred pore size, but does not indicate whether horizontal or vertical flow is being considered. As shown by Dai et al. (2019) and Yoneda et al. (2019a), the horizontal permeability for gas hydrate-bearing sediment in the primary Area B reservoir is approximately four times higher than the vertical permeability. As noted by Dai et al. (2017) and Fujii et al. (2015) for the Nankai Trough gas hydrate study, the relationship between NMR and core permeability measurements is not consistent and not fully understood. Caution is advised when making direct comparisons of the permeability magnitudes between NMR and other permeability measurements.

Nonetheless, the connection to LWD NMR permeability data is being made here to provide a means of assessing the permeability for NGHP-02-09, which penetrates the extremely coarse-grained, highly gas hydrate-saturate levee sediment on the opposite side of the channel from Site NGHP-02-08. There are no direct measurements of the seal sediment permeability for NGHP-02-09, but as shown in Waite et al. (2019), LWD NMR results show the overburden at Site NGHP-02-08 is approximately one order of magnitude more permeable than at Site NGHP-02-09 for the ~20 m of sediment directly above the main gas hydrate reservoir. Based on the NGHP-02-08 results showing the core-based permeability results being approximately one order of magnitude lower than the LWD NMR, a core-based estimate of the vertical permeability of the overburden directly in contact with the Site NGHP-02-09 gas hydrate reservoir would be 0.002 mD. This result supports the modeling assumption by Moridis et al. (2019) of a low-permeability upper contact for the gas hydrate reservoir.

5.2. Seal sediment impacts on fluid flows in gas production

When depressurization is applied for gas production from gas hydrate sediments, pore pressure in the production wells is dropped toward the target pressure, but reaching the target pressure is to some extent limited by the reservoir geometry (Terzariol et al., 2017). Ideally, the permeability of a seal layer is less than the permeability of the gas hydrate-bearing reservoir sediment, and much less than the permeability of the reservoir sediment after gas hydrate is lost via dissociation (see permeability of pressure cores from gas hydrate reservoirs in Yoneda et al. (2019a) and Boswell et al. (2019b)). This permeability difference between the seal and reservoir means the seal layer hinders vertical flow and promotes the horizontal, radial flow that is required for advancing the pressure gradient into the formation and sweeping out methane produced by dissociating gas hydrate (Ajayi et al., 2018). The permeability difference between reservoir and seal sediment can increase during production if, when the effective stress escalates due to pore pressure reduction, consolidation occurs in the seal sediment and constricts flow passages near the base of the seal layer, further lowering the seal permeability.

When gas hydrate dissociates, pure water is released that freshens the pore water (Hesse and Harrison, 1981). Fines are influenced by pore

fluid chemistry because fines are dominated by electrical-force interactions rather than the gravitational force. The arrangement, or fabric, of fines is sensitive to pore fluid chemistry, and is particularly influenced by salt concentration in pore fluid. Freshened water can alter the sediment fabric (Sridharan and Rao, 1973; Di Maio and Fenelli, 1994; Palomino and Santamarina, 2005; Jang and Santamarina, 2016), altering the sediment's mechanical properties as well as changing how easily the fines can be resuspended into the pore-water flow (Jang et al., 2018). These processes are particularly important for the seal sediment at the interface between the reservoir and overlying seal, where the fines fabric in the overlying seal can be disrupted both by the changing reservoir pore-fluid chemistry, and by the high flow rate of the production fluids. At the flow rates considered for production, Oyama et al. (2016) suggests the fabric becomes disrupted, causing some fines to become suspended in the moving pore fluid. Based on the clusters of fine particles observed in the SEM-EDS imagery (Fig. 8b), the Site NGHP-02-08 seal appears to contain electrically-sensitive clays that become more easily dislodged in the presence of fresh water and consequently have a negative impact on the reservoir permeability near the contact with the upper seal. 2D micromodel studies (Cao et al., 2019) suggest suspended fines associated with the NGHP-02-09 reservoir itself also have a relatively high potential for clogging pore throats.

5.3. Conservative shear strength parameter

Mechanical stability of gas hydrate reservoir systems during gas production can be partially evaluated through shear strength measurements. In general, shear strength values measured by direct shear tests are ~70% of those measured by triaxial compression tests (Mayne, 1985), meaning that estimates from direct shear tests may be conservative. One reason the direct shear results are conservative is that the nominal shear area is used for the shear strength calculation (ASTM D3080, 2011; Lambe, 1951), but shear only occurs over a portion of that area in a direct shear experiment. Calculating the shear strength with the actual shear area could increase the peak shear strength by 3% and the shear strength at the ultimate state by 19%.

Nonetheless, the direct shear approach is appropriate for NGHP-02 because when there is horizontal anisotropy in the reservoir system, and the anisotropy has the potential to restrict the shear failure plane to being horizontal (Fig. 8a), the shear strength measured by direct shear tests could represent the horizontal shear failure criteria (Bjerrum, 1973; Wroth, 1987). Another reason to consider using a conservative strength parameter estimate for the NGHP-02 reservoir modeling of the seal sediment is the presence of fractures or fissures. In this environment, a residual friction angle is preferred rather than a peak friction angle (Skempton, 1964). Since visualized resistivity images of LWD data provide evidence of many fractures in the seal layer (Collett et al., 2019; Waite et al., 2019), the proper friction angle for the seal layer should be close to the residual friction angle.

5.4. Core degradation during long-term storage

Two core degradation processes occurring during long-term core storage are 1) core sediment expansion due to the absence of an applied effective stress in the storage chamber, and 2) methane hydrate dissolution due to a lack of methane in the pressurizing fluid in contact with the sediment. Core expansion degradation can be reversed via the reapplication of the in situ effective stress prior to measuring the core's physical properties (Santamarina et al., 2015), though as shown here, the consolidation times required to fully reconsolidate fine-grained sediment can be lengthy. The loss of gas hydrate through dissolution cannot be reversed.

As shown in Fig. 3, V_p at the time of core recovery was above 2000 m/s at 247.6 mbsf, indicating the presence of a thin gas hydrate-bearing interval. Approximately a year later, in spite of the core remaining within the gas hydrate stability conditions defined by pressure and

temperature, the V_p profile through 247.6 mbsf closely followed the background, gas-hydrate-free trend. Because the core was pressurized with fresh, methane-free water, the core fluid was below the equilibrium methane saturation at the pressure and temperature conditions during transport and storage, and the methane hydrate dissolved to drive the pore-fluid methane concentration up toward the equilibrium value. Because the overall gas hydrate content of the core was low, the gas hydrate was completely consumed.

The same process will happen in all gas hydrate-bearing cores stored in this fashion. For cores stored with high gas hydrate saturations, there is less free water remaining that requires methane saturation, and there is also enough gas hydrate present to fully methane-saturate the free water without fully consuming the gas hydrate. It is generally not practical to pre-saturate the chamber pressurization fluid with methane, so to minimize gas hydrate loss, the core storage chamber should contain as little free fluid space as possible. Solid spacers should be added to a chamber prior to core loading if the core does not extend the full length of the chamber.

The equilibrium methane solubility in the presence of methane hydrate decreases only very slightly with increasing fluid pressure, but decreases significantly as the temperature falls away from the stability temperature (Lu et al., 2008; Servio and Englezos, 2002). Gas hydrate dissolution is minimized when cores are stored at temperatures as cold as possible without freezing the specimens. Freezing should be avoided because fluid expansion and gas exsolution during freezing significantly alters the sediment fabric, limiting what can be learned about the in situ environment. Practically speaking, gas hydrate saturations measured in cores stored long-term should be considered lower bounds on the in situ gas hydrate saturation.

6. Conclusions

The evaluation of natural gas hydrate reservoirs to ensure effective and safe gas production requires credible measurements of geological, geochemical, geophysical, and geomechanical parameters of the system. Pressure core technology can provide excellent means to retrieve natural gas-hydrate-bearing sediments while avoiding core disturbance from gas hydrate dissociation, and to measure and assess relevant physical and geomechanical properties of the in situ, gas hydrate-bearing environment. Even in the absence of gas hydrate, pressure coring protects the sediment from disturbance caused by the exsolution of dissolved gases. Pressure coring characterization tools then provide a means of directly manipulating the sediment and pore fluids to measure mechanical properties that dynamically change as methane is extracted from a gas hydrate-bearing reservoir.

This study uses a pressure core collected from the fine-grained seal layer just above the primary gas hydrate-bearing reservoir at Site NGHP-02-08 to provide geotechnical properties and to give insight into the role of the seal layer in the gas hydrate reservoir system defined by a buried channel levee environment. The effective stress chamber and direct shear chamber of the pressure core characterization tools were used here to measure geotechnical properties including compressibility, shear strength, and permeability. The seal layer is found to contain clayey sediments with high compressibility ($C_c = 0.262$), low peak shear strength (403 kPa) and low residual friction angle (8°) at the 2 MPa in situ vertical stress. The vertical permeability at the in situ stress is also low (consensus permeability = 0.02 mD), and this direct measurement helps resolve discrepancies between two indirect permeability measurement methods. The consensus permeability result is an order of magnitude lower than the empirical remote sensing estimate from LWD NMR, and two orders of magnitude higher than an empirical estimate based on a sediment index property assessment.

This seal sediment, being so near the contact with the primary reservoir sediment and containing electrically-sensitive fines, would likely be influenced and disturbed by gas hydrate dissociation conditions imposed on the reservoir via two mechanisms: 1) depressurization

methods can change the effective stress; 2) gas hydrate dissociation affects pore water chemistry. Sediment stability parameters such as shear strength and friction angle should therefore be conservatively selected for the safety of the reservoir system.

Although pressure coring maintains the hydrostatic (pore) pressure and temperature within the gas hydrate stability field, the loss of effective stress and the fresh water used to pressurize the specimen do degrade the specimen over time. For post-cruise pressure core analyses, the following disturbance remediation approaches are recommended: 1) core storage temperatures just above freezing will minimize the pore-water methane solubility and reduce gas hydrate dissolution; 2) after pressure coring, and again just prior to destructively testing the core sediment, non-destructive measurements such as V_p , density and X-ray images should be obtained to indicate the extent of physical alterations in core conditions during long-term storage and provide important support for interpreting measured results; 3) physical property testing should be accomplished at least at the in situ effective stress to remove the core degradation due to the core expansion occurring in the absence of a vertical effective stress during core storage. Ideally, pressure core storage prior to the pressure core analyses would be brief to minimize the sampling disturbance driven by long-term sediment structure and phase changes during storage.

Acknowledgements

The author(s) wish to thank those that contributed to the success of the National Gas Hydrate Program Expedition 02 (NGHP-02). NGHP-02 was planned and managed by the Oil and Natural Gas Corporation Limited India (ONGC) on the behalf of the India National Gas Hydrate Program through Directorate General of Hydrocarbons (DGH) under the Ministry of Petroleum and Natural Gas (India). The drilling platform, *D/V Chikyu*, was operated by the Japanese Drilling Company (JDC) and the shipboard science program was managed by the Japan Agency for Marine-Earth Science and Technology (JAMSTEC). LWD, wireline logging, and formation testing services were provided by Schlumberger. Pressure coring tools were provided by JAMSTEC, and shipboard pressure core operations and analysis were provided by Geotek Coring. Additional operational and scientific support was provided by the U.S. Geological Survey (USGS), the U.S. Department of Energy (US-DOE), the National Institute of Advanced Industrial Science and Technology (AIST), and the Japan Oil, Gas and Metals National Corporation (JOGMEC). The financial support for the NGHP-02, from the Oil Industry Development Board, Oil and Natural Gas Corporation Limited is gratefully acknowledged. We also acknowledge the support extended by all the participating organizations of the NGHP: MoP&NG, DGH, ONGC, GAIL, OIL, NIO, and NIOT. This work was also supported by the Energy, and the Coastal and Marine Science Programs of the U.S. Geological Survey, with additional funding from US-DOE Interagency Agreement DE-FE00-23495. The authors wish to thank J. Pohlman and M. Casso (USGS) for performing the gas analysis for this study, and C. Ruppel (USGS) for constructive comments on the manuscript. This report was prepared as an account of work sponsored by an agency of the United States Government. Any use of trade, firm or product name is for descriptive purposes only and does not imply endorsement by the Japanese or U.S. Government.

References

Ajayi, T., Anderson, B.J., Seol, Y., Boswell, R., Myshakin, E.M., 2018. Key aspects of numerical analysis of gas hydrate reservoir performance: Alaska North Slope Prudhoe Bay Unit "L-Pad" hydrate accumulation. *J. Nat. Gas Sci. Eng.* 51, 37–43.

ASTM, 2010. Standard Test Methods for Measurement of Hydraulic Conductivity of Saturated Porous Materials Using a Flexible Wall Permeameter. ASTM D5084. West Conshohocken, PA.

ASTM, 2011. Standard Test Method for Direct Shear Test of Soils under Consolidated Drained Conditions. ASTM D3080. West Conshohocken, PA.

Ballard, A.L., Sloan, E.D., 2004. The next generation of hydrate prediction - Part III. Gibbs energy minimization formalism. *Fluid Phase Equil.* 218 (1), 15–31.

Bjerrum, L., 1973. Problems of soil mechanics and construction on soft clays and structurally unstable soils. In: *Proceedings of the Eighth International Conference on Soil Mechanics and Foundation Engineering, Moscow*. 3. pp. 111–159.

Bohannon, J., 2008. Energy - weighing the climate risks of an untapped fossil fuel. *Science* 319 (5871) 1753–1753.

Bolt, G.H., 1956. Physico-chemical analysis of the compressibility of pure clays. *Geotechnique* 6 (2), 86–93.

Boswell, R., Myshakin, E., Moridis, G., Konno, Y., Collett, T., Reagan, M., Ajayi, T., Seol, Y., 2019a. India National Gas Hydrate Program Expedition 02 summary of scientific results: numerical simulation of reservoir response to depressurization. *J. Mar. Pet. Geol.* 108, 154–166.

Boswell, R., et al., 2019b. India National Gas Hydrate Program Expedition 02 summary of scientific results: evaluation of natural gas-hydrate-bearing pressure cores. *J. Mar. Pet. Geol.* 108, 143–153.

Brooks, R.H., Corey, A.T., 1964. Hydraulic properties of porous media. Colorado State University (Fort Collins) Hydrology Paper No. 3.

Burland, J.B., 1990. 30th rankine lecture - on the compressibility and shear-strength of natural clays. *Geotechnique* 40 (3), 329–378.

Cao, S.C., Jang, J., Jung, J., Waite, W.F., Collett, T.S., Kumar, P., 2019. 2D micromodel study of clogging behavior of fine-grained particles associated with gas hydrate production in NGHP-02 gas hydrate reservoir sediments. *J. Mar. Pet. Geol.* 108, 714–730.

Carrier, W.D., 2003. Goodbye, hazen; hello, kozeny-carman. *J. Geotech. Geoenviron. Eng.* 129 (11), 1054–1056.

Cerato, A.B., Lutenecker, A.J., 2004. Determining intrinsic compressibility of fine-grained soils. *J. Geotech. Geoenviron. Eng.* 130 (8), 872–877.

Chen, B.S., Mayne, P.W., 1994. Profiling the Overconsolidation Ratio of Clays by Piezocone Tests. GIT-CEEEO-94-1. Arlington, vol. A.

Collett, T.S., Johnson, A.H., Knapp, C.C., Boswell, R., 2009. Natural gas hydrates: a review. In: Collett, T.S., Johnson, A.H., Knapp, C.C., Boswell, R. (Eds.), *Natural Gas Hydrates - Energy Resource Potential and Associated Geologic Hazards*, vol. 89. AAPG Memoir, pp. 146–219.

Collett, T.S., Boswell, R., Waite, W.F., Kumar, P., Roy, S.K., Chopra, K., Singh, S.K., Yamada, Y., Tenma, N., Pohlman, J., Zryanova, M., NGHP Expedition 02 Scientific Party, 2019. India National Gas Hydrate Program Expedition 02 summary of scientific results: gas hydrate systems along the eastern continental margin of India. *J. Mar. Petrol. Geol.* 108, 39–142.

Dai, S., Boswell, R., Waite, F.W., Jang, J., Lee, J.Y., Seol, Y., 2017. What has been learned from pressure cores. In: *The 9th International Conference on Gas Hydrates, Denver, Colorado, USA, June 25-30, 2017*.

Dai, et al., 2019. Permeability anisotropy and relative permeability in sediments from the National Gas Hydrate Program Expedition 02, offshore India. *J. Mar. Pet. Geol.* 108, 705–713.

Dai, S., Santamarina, J.C., 2014. Sampling disturbance in hydrate-bearing sediment pressure cores: NGHP-01 expedition, Krishna-Godavari Basin example. *Mar. Petrol. Geol.* 58, 178–186.

Daigle, H., Dugan, B., 2009. Extending NMR data for permeability estimation in fine-grained sediments. *Mar. Petrol. Geol.* 26 (8), 1419–1427.

Daigle, H., Dugan, B., 2011. An improved technique for computing permeability from NMR measurements in mudstones. *J. Geophys. Res. Solid Earth* 116.

Di Maio, C., Fenelli, G.B., 1994. Residual strength of kaolin and bentonite - the influence of their constituent pore fluid. *Geotechnique* 44 (2), 217–226.

Dickens, G., 2001. On the fate of past gas: what happens to methane released from a bacterially mediated gas hydrate capacitor? G-cubed 2 2000GC000131.

Dixit, et al., 2019. Origin of gas in gas hydrates as interpreted from geochemistry data obtained during the National Gas Hydrate Program Expedition 02, Krishna Godavari Basin, offshore India. *J. Mar. Pet. Geol.* 108, 386–396.

Fujii, T., Suzuki, K., Takayama, T., Tamaki, M., Komatsu, Y., Konno, Y., Yoneda, J., Yamamoto, K., Nagao, J., 2015. Geological setting and characterization of a methane hydrate reservoir distributed at the first offshore production test site on the Daini-Atsumi Knoll in the eastern Nankai Trough, Japan. *Mar. Petrol. Geol.* 66, 310–322.

Hesse, R., Harrison, W.E., 1981. Gas hydrates (clathrates) causing pore-water freshening and oxygen isotope fractionation in deep-water sedimentary sections of terrigenous continental margins. *Earth Planet Sci. Lett.* 55 (3), 453–462.

Holland, et al., 2019. Gas hydrate saturation and morphology from analysis of pressure cores acquired in the Bay of Bengal during expedition NGHP-02, offshore India. *J. Mar. Pet. Geol.* 108, 407–423.

Jang, J., Cao, S.C., Stern, L.A., Jung, J., Waite, F.W., 2018. Impact of pore fluid chemistry on fine-grained sediment fabric and compressibility. *J. Geophys. Res. Solid Earth* 123, 5495–5514.

Jang, J., Dai, S., Yoneda, J., Waite, F.W., Stern, L.A., Boze, L.-G., Collett, T.S., Kumar, P., 2018. Pressure core analysis of geomechanical and fluid flow properties of seals associated with gas hydrate-bearing reservoirs in the Krishna-Godavari Basin, offshore India. *J. Mar. Pet. Geol.* 108, 537–550.

Jang, J., Santamarina, J.C., 2016. Fines classification based on sensitivity to pore-fluid chemistry. *J. Geotech. Geoenviron. Eng.* 142 (4), 06015018.

Jang, J., Waite, W.F., Stern, L., Collett, T.S., Kumar, P., 2019. Physical property characteristics of gas hydrate-bearing reservoir and associated seal sediments collected during NGHP-02 in the Krishna-Godavari Basin, in the offshore of India. *J. Mar. Pet. Geol.* 108, 249–271.

Johns, M.W., Taylor, E., Bryant, W.R., 1982. Geotechnical sampling and testing of gas-charged marine sediments at in situ pressure. *Geo Mar. Lett.* 2 (3–4), 231–236.

Kim, J., Dai, S., Jang, J., Waite, F.W., Collett, T.S., 2019. Compressibility and particle crushing of Krishna-Godavari Basin sediments from offshore India: Implications for gas production from deep-water gas hydrate deposits. *J. Mar. Pet. Geol.* 108, 697–704.

- Kumar, P., Collett, T.S., et al., 2019. India National Gas Hydrate Program Expedition 02-operational and technical summary. *J. Mar. Pet. Geol.* 108, 3–38.
- Kurihara, M., Sato, A., Funatsu, K., Ouchi, H., Masuda, Y., Narita, H., Collett, T.S., 2011. Analysis of formation pressure test results in the Mount Elbert methane hydrate reservoir through numerical simulation. *Mar. Petrol. Geol.* 28 (2), 502–516.
- Kvenvolden, K., 1993. Gas hydrates - geological perspective and global change. *Rev. Geophys.* 31 (2), 173–187.
- Lambe, T.W., 1951. *Soil Testing for Engineers*. John Wiley & Sons, Inc.
- Lin, J.S., Uchida, S., Myshakin, E., Seol, Y., Rutqvist, J., Boswell, R., 2019. Assessing the geomechanical stability of interbedded hydrate-bearing sediments under gas production by depressurization at site NGHP-02-16. *J. Mar. Pet. Geol.* 108, 648–659.
- Lu, W.J., Chou, I.M., Burruss, R.C., 2008. Determination of methane concentrations in water in equilibrium with sl methane hydrate in the absence of a vapor phase by in situ Raman spectroscopy. *Geochem. Cosmochim. Acta* 72 (2), 412–422.
- Lupini, J.F., Skinner, A.E., Vaughan, P.R., 1981. The drained residual strength of cohesive soils. *Geotechnique* 31 (2), 181–213.
- Mayne, P.W., 1985. A review of undrained strength in direct simple shear. *Soils Found.* 25 (3), 64–72.
- Mesri, G., 1989. A Reevaluation of $s_{u(mob)} = 0.22\sigma'_p$ using laboratory shear tests. *Can. Geotech. J.* 26 (1), 162–164.
- Mesri, G., Cepedadi, A.F., 1986. Residual shear-strength of clays and shales. *Geotechnique* 36 (2), 269–274.
- Mesri, G., Olson, R.E., 1970. Shear strength of montmorillonite. *Geotechnique* 20 (3), 261–270.
- Mitchell, J.K., Soga, K., 2005. *Fundamentals of Soil Behavior*. John Wiley & Sons, Inc.
- Moridis, G.J., Reagan, M.T., Quiérua, A.F., Boswell, R., 2019. Evaluation of the performance of the oceanic hydrate accumulation at site NGHP-02-09 in the Krishna-Godavari Basin during a production test and during single and multi-well production scenarios. *J. Mar. Pet. Geol.* 108, 660–696.
- Myshakin, E.M., Seol, Y., Lin, J.S., Uchida, S., Collett, T.S., Boswell, R., 2019. Numerical simulations of depressurization-induced gas production from an interbedded turbidite gas hydrate-bearing sedimentary section in the offshore India: Site NGHP-02-16 (Area-B). *J. Mar. Petrol. Geol.* 108, 619–638.
- Nanda, J., Shukla, K., Lall, M.V., Yadav, U.S., Kumar, P., 2019. Lithofacies characterization of gas hydrate prospects discovered during the National Gas Hydrate Program Expedition 02, offshore Krishna-Godavari Basin, India. *J. Mar. Pet. Geol.* 108, 226–238.
- NAVFAC, 1986. *Soil Mechanics, Design Manual 7.01*. Naval Facilities Engineering Command, Alexandria, VA.
- Oshima, M., et al., 2019. Lithological properties of natural gas hydrate-bearing sediments in pressure-cores recovered from the Krishna-Godavari Basin. *J. Mar. Pet. Geol.* 108, 439–470.
- Oyama, H., Abe, S., Yoshida, T., Sato, T., Nagao, J., Tenma, N., Narita, H., 2016. Experimental study of mud erosion at the interface of an artificial sand-mud alternate layer. *J. Nat. Gas Sci. Eng.* 34, 1106–1114.
- Palomino, A.M., Santamarina, J.C., 2005. Fabric map for kaolinite: effects of pH and ionic concentration on behavior. *Clay Clay Miner.* 53 (3), 209–222.
- Priest, J.A., Druce, M., Roberts, J., Schultheiss, P., Nakatsuka, Y., Suzuki, K., 2015. PCATS Triaxial: a new geotechnical apparatus for characterizing pressure cores from the Nankai Trough, Japan. *Mar. Petrol. Geol.* 66, 460–470.
- Priest, J., Hayley, J., Smith, W., Schultheiss, P., Roberts, J., 2019. PCATS triaxial testing: geomechanical properties of sediments from pressure cores recovered from the Bay of Bengal during expedition NGHP-02. *J. Mar. Pet. Geol.* 108, 424–438.
- Reagan, M.T., Moridis, G.J., 2008. Dynamic response of oceanic hydrate deposits to ocean temperature change. *J. Geophys. Res. Oceans* 113 (C12).
- Ren, X.W., Santamarina, J.C., 2018. The hydraulic conductivity of sediments: a pore size perspective. *Eng. Geol.* 233, 48–54.
- Ruppel, C.D., Kessler, J.D., 2017. The interaction of climate change and methane hydrates. *Rev. Geophys.* 55 (1), 126–168.
- Santamarina, J.C., Dai, S., Jang, J., Terzariol, M., 2012. Pressure core characterization tools for hydrate-bearing sediments. *Sci. Drill.* 14, 44–48.
- Santamarina, J.C., Dai, S., Terzariol, M., Jang, J., Waite, W.F., Winters, W.J., Nagao, J., Yoneda, J., Konno, Y., Fujii, T., Suzuki, K., 2015. Hydro-bio-geomechanical properties of hydrate-bearing sediments from Nankai Trough. *Mar. Petrol. Geol.* 66, 434–450.
- Santamarina, J.C., Klein, K.A., Wang, Y.H., Prencke, E., 2002. Specific surface: determination and relevance. *Can. Geotech. J.* 39, 233–241.
- Schultheiss, P.J., Francis, T.J.G., Holland, M., Roberts, J.A., Amann, H., Thjunjoto, Parke, R.J., 2006. Pressure coring, logging and subsampling with the HYCINTH system. In: Rothwell, G. (Ed.), *New Techniques in Sediment Core Analysis*. 267. pp. 151–163 (Geol. Soc. London, Spec. Pub).
- Servio, P., Englezos, P., 2002. Measurement of dissolved methane in water in equilibrium with its hydrate. *J. Chem. Eng. Data* 47 (1), 87–90.
- Shukla, K.M., Kumar, P., Yadav, U.S., NGHP-02 Science team, 2019a. Gas hydrate reservoir identification, delineation, and characterization in the Krishna-Godavari basin using subsurface geologic and geophysical data from the National Gas Hydrate Program 02 Expedition, offshore India. *J. Mar. Pet. Geol.* 108, 185–205.
- Shukla, et al., 2019b. National Gas Hydrate Program Expedition 02: Identification of gas hydrate prospects in the Krishna-Godavari Basin, Offshore India. *J. Mar. Pet. Geol.* 108, 167–184.
- Skempton, A.W., 1964. Long-term stability of clay slopes. *Geotechnique* 14 (2), 75–101.
- Sloan, E.D., Koh, C.A., 2007. *Clathrate Hydrates of Natural Gases*. CRC Press, Taylor & Francis Group, LLC, New York.
- Sridharan, A., Nagaraj, H.B., 2000. Compressibility behaviour of remoulded, fine-grained soils and correlation with index properties. *Can. Geotech. J.* 37, 712–722.
- Sridharan, A., Rao, G.V., 1973. Mechanisms controlling volume change of saturated clays and role effective stress concept. *Geotechnique* 23 (3), 359–382.
- Taylor, D.W., 1948. *Fundamentals of Soil Mechanics*. John Wiley & Sons, Inc., New York.
- Terzaghi, K., Peck, R.B., Mesri, G., 1996. *Soil Mechanics in Engineering Practice*. John Wiley & Sons, Inc., New York.
- Terzariol, M., Goldsztein, G., Santamarina, J.C., 2017. Maximum recoverable gas from hydrate bearing sediments by depressurization. *Inside Energy* 141, 1622–1628.
- Tiwari, B., Ajmera, B., 2011. Consolidation and swelling behavior of major clay minerals and their mixtures. *Appl. Clay Sci.* 54 (3–4), 264–273.
- Todd, T., Simmons, G., 1972. Effect of pore pressure on velocity of compressional waves in low-porosity rocks. *J. Geophys. Res.* 77 (20), 3731–3743.
- Waite, W., Jang, J., Collett, T., Kumar, P., 2019. Downhole physical property-based description of a gas hydrate petroleum system in NGHP-02 Area C: A channel, Levee, Fan complex in the Krishna-Godavari basin offshore India. *J. Mar. Pet. Geol.* 108, 272–295.
- Wroth, C.P., 1987. The behavior of normally consolidated clay as observed in undrained direct shear tests. *Geotechnique* 37 (1), 37–43.
- Yoneda, J., Masui, A., Konno, Y., Jin, Y., Egawa, K., Kida, M., Ito, T., Nagao, J., Tenma, N., 2015. Mechanical behavior of hydrate-bearing pressure-core sediments visualized under triaxial compression. *Mar. Petrol. Geol.* 66, 451–459.
- Yoneda, J., Masui, A., Konno, Y., Jin, Y., Kida, M., Katagiri, J., Nagao, J., Tenma, N., 2017. Pressure-core-based reservoir characterization for geomechanics: insights from gas hydrate drilling during 2012–2013 at the eastern Nankai Trough. *Mar. Petrol. Geol.* 86, 1–16.
- Yoneda, et al., 2019a. Permeability variation and anisotropy of gas hydrate-bearing pressure-core sediments recovered from the Krishna-Godavari Basin, offshore India. *J. Mar. Pet. Geol.* 108, 524–536.
- Yoneda, Y., Oshima, M., Kida, M., Kato, A., Konno, Y., Jin, Y., Tenma, N., Waite, W., Jang, J., 2019b. Pressure core based onshore laboratory analysis on mechanical properties of hydrate-bearing sediments recovered during India's National Gas Hydrate Program Expedition (NGHP) 02. *J. Mar. Pet. Geol.* 108, 482–501.
- Yoneda, J., Masui, A., Konno, Y., Jin, Y., Kida, M., Katagiri, J., Nagao, J., Tenma, N., 2019c. Consolidation and hardening behavior of hydrate-bearing pressure core sediments under high confining pressure based on natural core sample from NGHP-02. *J. Mar. Pet. Geol.* 108, 512–523.
- Young, D.F., Munson, B.R., Okiiishi, T.H., Huebsch, W.W., 2007. *A Brief Introduction to Fluid Mechanics*. John Wiley & Sons, Inc, York, PA.
- Yun, T.S., Fratta, D., Santamarina, J.C., 2010. Hydrate-bearing sediments from the Krishna-Godavari Basin: physical characterization, pressure core testing, and scaled production monitoring. *Energy Fuels* 24 (11), 5972–5983.
- Yun, T.S., Lee, C., Lee, J.S., Bahk, J.J., Santamarina, J.C., 2011. A pressure core based characterization of hydrate-bearing sediments in the Ulleung Basin, Sea of Japan (East Sea). *Journal of Geophysical Research-Solid Earth* 116.
- Yun, T.S., Narsilio, G.A., Santamarina, J.C., 2006. Physical characterization of core samples recovered from Gulf of Mexico. *Mar. Petrol. Geol.* 23 (9–10), 893–900.